



HAL
open science

Mineral characterization of the biogenic Fe(III)(hydr)oxides produced during Fe(II)-driven denitrification with Cu, Ni and Zn

Kyriaki Kiskira, Stefano Papirio, Maria Cristina Mascolo, Chloé Fourdrin, Yoan Pechaud, Eric D. van Hullebusch, Giovanni Esposito

► **To cite this version:**

Kyriaki Kiskira, Stefano Papirio, Maria Cristina Mascolo, Chloé Fourdrin, Yoan Pechaud, et al.. Mineral characterization of the biogenic Fe(III)(hydr)oxides produced during Fe(II)-driven denitrification with Cu, Ni and Zn. *Science of the Total Environment*, 2019, 687, pp.401 - 412. 10.1016/j.scitotenv.2019.06.107 . hal-03484507

HAL Id: hal-03484507

<https://hal.science/hal-03484507>

Submitted on 20 Dec 2021

HAL is a multi-disciplinary open access archive for the deposit and dissemination of scientific research documents, whether they are published or not. The documents may come from teaching and research institutions in France or abroad, or from public or private research centers.

L'archive ouverte pluridisciplinaire **HAL**, est destinée au dépôt et à la diffusion de documents scientifiques de niveau recherche, publiés ou non, émanant des établissements d'enseignement et de recherche français ou étrangers, des laboratoires publics ou privés.



Distributed under a Creative Commons Attribution - NonCommercial 4.0 International License

1 **Mineral characterization of the biogenic Fe(III)(hydr)oxides produced**
2 **during Fe(II)-driven denitrification with Cu, Ni and Zn**

3
4 Kyriaki Kiskira^{1,2,*}, Stefano Papirio³, Maria Cristina Mascolo¹, Chloé Fourdrin², Yoan
5 Pechaud², Eric D. van Hullebusch^{2,4}, Giovanni Esposito³

6

7 ¹ *Department of Civil and Mechanical Engineering, University of Cassino and Southern*
8 *Lazio, Via Di Biasio 43, 03043 Cassino (FR), Italy.*

9 ² *Université Paris-Est, Laboratoire Géomatériaux et Environnement (LGE), EA 4508,*
10 *UPEM, 77454 Marne-la-Vallée, France.*

11 ³ *Department of Civil, Architectural and Environmental Engineering, University of Napoli*
12 *Federico II, Via Claudio 21, 80125, Napoli, Italy.*

13 ⁴ *IHE Delft Institute for Water Education, Department of Environmental Engineering and*
14 *Water Technology, P.O. Box 3015, 2601 DA Delft, the Netherlands.*

15

16 ***Corresponding author**

17 Kyriaki Kiskira

18 Phone: +39 0776 299 4717

19 Email: kirki.kis@gmail.com

20 Present address: Department of Civil and Mechanical Engineering, University of Cassino
21 and Southern Lazio, Via Di Biasio 43, 03043 Cassino (FR), Italy

1 **Abstract**

2 The recovery of iron and other heavy metals by the formation of Fe(III) (hydr)oxides is an important
3 application of microbially-driven processes. The mineral characterization of the precipitates formed
4 during Fe(II)-mediated autotrophic denitrification with and without the addition of Cu, Ni, and Zn
5 by four different microbial cultures was investigated by X-ray fluorescence (XRF), Raman
6 spectroscopy, scanning electron microscopy equipped with energy dispersive X-Ray analyzer
7 (SEM-EDX), Fourier transform infrared spectroscopy (FTIR) and X-ray Powder Diffraction (XRD)
8 analyses. Fe(II)-mediated autotrophic denitrification resulted in the formation of a mixture of Fe(III)
9 (hydr)oxides composed of amorphous phase, poorly crystalline (ferrihydrite) and crystalline phases
10 (hematite, akaganeite and maghemite). The use of a *Thiobacillus*-dominated mixed culture enhanced
11 the formation of akaganeite, while activated sludge enrichment and the two pure cultures of *T.*
12 *denitrificans* and *Pseudogulbenkiania* strain 2002 mainly resulted in the formation of maghemite.
13 The addition of Cu, Ni and Zn led to similar Fe(III) (hydr)oxides precipitates, probably due to the
14 low metal concentrations. However, supplementing Ni and Zn slightly stimulated the formation of
15 maghemite. A thermal post-treatment performed at 650°C enhanced the crystallinity of the
16 precipitates and favored the formation of hematite and some other crystalline forms of Fe associated
17 with P, Na and Ca.

18

19 **Keywords:** ferrous iron, nitrate, autotrophic denitrification, heavy metals, biorecovery

20 **1. Introduction**

21 The need for iron and other metals from secondary sources is nowadays gaining increasing
22 attention. Most of the recovery options currently used is not economically feasible and, therefore, it
23 is critical to develop low-cost and environmental-friendly methods to recover metals from
24 wastewaters (Pat-Espadas and Cervantes, 2018). Fe(II)-mediated autotrophic denitrification is a
25 promising biotechnology to be employed for iron recovery when nitrogen and metal contamination
26 coexists. Chemoautotrophic denitrifiers are capable of coupling Fe(II) oxidation with denitrification
27 resulting in the bioreduction of nitrate to nitrogen gas and the production of Fe(III) precipitates,
28 which can be subsequently removed and recovered (Kiskira et al., 2017a). Different biogenic
29 Fe(III)(hydro)oxide mineral phases such as goethite, lepidocrocite, hematite, magnetite, maghemite,
30 2-line ferrihydrite and mixed-phase Fe(II)-Fe(III) minerals (i.e. green rust) have been reported as
31 potential Fe-based products from Fe(II)-driven denitrification (Senko et al., 2005a, b; Weber et al.,
32 2006; Konhauser et al., 2011).

33 A lot of environmental and operating parameters affect the formation of Fe(III) precipitates.
34 Among them, the use of different microbial species and their metabolic rates significantly result in
35 diverse biogenic Fe(III) (oxyhydr)oxide minerals from soluble Fe(II) (Posth et al., 2014). Other
36 factors are the medium composition, the concentration of possible co-substrates, the incubation
37 conditions and the presence of nucleation sites (Kappler and Straub, 2005; Senko et al., 2005a;
38 Larese-Casanova et al., 2010; Pantke et al., 2012). A slower Fe(II) oxidation rate produces
39 crystalline minerals, such as goethite, while a rapid Fe(II) oxidation rate leads to the formation of
40 less crystallized phases such as ferrihydrite (Lack et al., 2002; Senko et al., 2005b). pH is another
41 factor that affects the formation and composition of Fe(III) precipitates. For instance, goethite

42 formation was reported at pH 7.7, while the production of lepidocrocite occurred at pH 6.3 in the
43 presence of *Acidovorax* sp. BoFeN1 (Larese-Casanova et al., 2010).

44 Due to their larger specific surface area and higher binding energy, biogenic oxides are more
45 efficient for the recovery of other metals and metalloids than chemically produced oxides through
46 co-precipitation or adsorption mechanisms (Hennebel et al., 2009). For instance, arsenic (As) has
47 been reported to effectively co-precipitate with biogenic goethite and lepidocrocite (Senn and
48 Hemond, 2002; Hohmann et al., 2009; Ahoranta et al., 2016; Xiu et al., 2016), with As being
49 adsorbed after its oxidation from As(III) to As(V) (Papiro et al., 2014). The microbial oxidation of
50 As(III) and Fe(II) linked to denitrification resulted in an enhanced immobilization of As(V) onto
51 biogenic Fe(III) (hydr)oxides in sand-packed bed columns (Sun et al., 2009). Pantke et al. (2012)
52 reported that green rust is a highly reactive iron mineral and can be used for the recovery of
53 chromium (Cr) and arsenic. Furthermore, Fe(III) oxides can be recycled and used for phosphorus
54 removal (Nielsen and Nielsen, 1998; Zhang et al., 2015).

55 The determination of the mineral identity of the Fe(III) precipitates formed is crucial in order
56 to decide the adoption of the “reuse strategy” and the possible applications (Velenturf and Jopson,
57 2019). Iron oxides are valuable minerals for many applications due to their low cost, abundance and
58 physico-chemical properties (Pouran et al., 2014; dos Santos et al., 2016). Among Fe(III)
59 (hydr)oxides, hematite, maghemite, magnetite and goethite have the greatest interest in industry
60 (Cao et al., 2015). Some of the major applications of recovered biogenic Fe(III) minerals are the
61 production of pigments for paints and the construction industry, magnetic pigments and ferrites,
62 catalysts for industrial synthesis, photo-chemicals and fertilizers, heavy metals immobilization,
63 adsorbents for water and gas purification as well as radioactive waste decontamination (Cornell and
64 Schwertmann, 2003; Chen et al., 2017; Fajardo et al., 2019).

65 A lack of knowledge exists on the mineralogical characterization of the precipitates
66 produced during Fe(II)-mediated autotrophic denitrification by different microbial species. Indeed,
67 most of the studies only dealt with the use of a single microbial culture, or did not investigate a
68 strategy to evaluate the potential of biogenic Fe(III) precipitates to incorporate other metals (Kiskira
69 et al., 2017a). To the best of authors' knowledge, only one study besides this investigated the
70 removal of other metals/metalloids (i.e. As) through the use of biogenic Fe(III) precipitates obtained
71 by Fe(II)-driven denitrification (Sun et al., 2009). In addition, this study is the first proposing the use
72 of a thermal post-treatment of amorphous phases or poorly crystalline biogenic Fe(III) precipitates
73 to increase their crystallinity, depending on their reuse strategy.

74 In particular, the objectives of this work were to: a) evaluate and characterize the different
75 Fe(III) precipitates produced using different microbial inocula by different mineral characterization
76 methods, i.e. X-ray Powder Diffraction (XRD), X-ray fluorescence (XRF), Raman spectroscopy,
77 scanning electron microscopy equipped with an energy dispersive X-Ray analyzer (SEM-EDX) and
78 Fourier transformation infrared spectroscopy (FTIR); b) use a thermal post-treatment to improve the
79 crystallinity of the precipitates; c) investigate the potential adsorption/co-precipitation of Cu, Ni and
80 Zn on Fe(III) precipitates.

81

82 **2. Materials and methods**

83 **2.1. Sources of microorganisms and mineral growth media**

84 Fe(III) precipitates were obtained from the batch experiments carried out by Kiskira et al.
85 (2018) with four chemolithotrophic denitrifying cultures in serum bottles. A *Thiobacillus*-dominated
86 mixed culture, previously used in experiments with thiosulfate (Di Capua et al., 2016; Zou et al.,

87 2016) and Fe(II) (Kiskira et al., 2017b) as electron donors, and an activated sludge enrichment,
88 originally collected from the municipal wastewater treatment plant in Cassino (Italy), were used as
89 mixed bacterial consortia. *Pseudogulbenkiania* sp. 2002 (DSM 18807) and *T. denitrificans* (DSM
90 12475) were obtained from the 'Leibniz-Institute DSMZ - German collection of microorganisms
91 and cell cultures' and used as pure cultures. All the cultures were supplemented to the serum bottles
92 with a 10% (v/v) amount. The initial concentration of *Thiobacillus*-mixed, *T. denitrificans* pure,
93 activated sludge and *Pseudogulbenkiania* sp. 2002 cultures in terms of volatile suspended solids
94 (VSS) was 200, 320, 410 and 750 mg VSS/L (Kiskira et al., 2018).

95 The denitrification potential of all cultures with Fe(II) was preliminarily evaluated in the
96 absence (Kiskira et al., 2017b) and in the presence of Cu, Ni and Zn (Kiskira et al., 2018) in
97 experiments performed at room temperature (i.e. $22 \pm 2^\circ\text{C}$), under helium atmosphere and with an
98 initial pH of 7.0. A circumneutral pH was maintained along the 10-days experiments due to the 2
99 g/L NaHCO_3 provided as both buffer and inorganic carbon source. Therefore, in this study the effect
100 of pH on the formation and composition of Fe(III) precipitates was not investigated. In addition to
101 NaHCO_3 , the basal medium also contained (g/L) 0.25 NH_4Cl , 0.30 KH_2PO_4 , 0.40 K_2HPO_4 , and 0.10
102 NaCl . The trace elements solution was added from a sterile stock solution as described in Weber et
103 al. (2001). Cu, Ni and Zn were added in concentration of 40 mg/L in the form of copper chloride
104 (CuCl_2), nickel chloride ($\text{NiCl}_2 \cdot 6\text{H}_2\text{O}$) and zinc chloride (ZnCl_2), all purchased from Sigma Aldrich
105 (Germany). The feed Fe(II) and NO_3^- concentrations were 600 and 120 mg/L, supplemented in the
106 form of iron(II) chloride ($\text{FeCl}_2 \cdot 4\text{H}_2\text{O}$) and sodium nitrate (NaNO_3), respectively.

107 **2.2. Sample preparation and analytical methods**

108 The mineral characterization of the Fe(III) precipitates formed during Fe(II)-mediated
109 autotrophic denitrification was performed on: i) four samples obtained in the absence of metals, with

110 the use of the *Thiobacillus*-dominated mixed culture (TM), *T. denitrificans* (TDP), activated sludge
111 enrichment (AS) and *Pseudogulbenkiania* strain 2002 (PG); ii) twelve samples obtained in the
112 experiments with Cu (TMC, TDPC, ASC, PGC), Ni (TMN, TDPN, ASN, PGN) and Zn (TMZ,
113 TDPZ, ASZ, PGZ). Furthermore, the precipitates from abiotic control (AC) experiments without
114 metals (Cu, Ni and Zn) were also characterized. Abiotic controls were also performed with the
115 addition of Cu, Ni and Zn as described by Kiskira et al. (2018), but the authors observed an 80%
116 lower precipitation of metals in the abiotic controls than that achieved in the biotic tests. Due to that,
117 the precipitates obtained in the abiotic controls with Cu, Ni and Zn were not analyzed in this study
118 because considered similar to those from abiotic tests without metals.

119 All the Fe(III)(hydr)oxides production tests were performed in duplicate. The precipitates
120 obtained from two duplicates were mixed prior to being analyzed with the different methods due to
121 the limited amount of precipitate obtained in each bottle. Afterwards, Fe(III) oxides were
122 pasteurized (80°C for 10 min), collected by centrifugation under anaerobic conditions, and washed
123 twice with a NaHCO₃ buffer (pH 6.8) as previously described (Weber et al., 2001). Then, the
124 precipitates were washed several times with double-distilled water by centrifugation, in order to
125 remove the impurity ions associated with the procedure, as described by Schwertmann and Cornell
126 (2000). Finally, the samples were dried at 40°C for 48 h prior to analysis.

127 **2.2.1. X-ray fluorescence, scanning electron microscopy and x-ray diffraction analyses**

128 The samples were firstly analyzed by using X-ray fluorescence (XRF) with a Niton XL3t
129 GOLDD + XRF analyzer (Thermo Fisher Scientific, USA) with ± 0.50 weight % precision in
130 measurement. The loose powder method was chosen to analyze these samples, as described in detail
131 by Takahashi (2015). The morphology of the samples after sputter coating with Au was also
132 examined by scanning electron microscopy (SEM) using an XL series microscope (Philips, The

133 Netherlands). Additionally, SEM-EDX analysis was performed with a Vega 3 microscope
134 (TESCAN, Czech Republic), equipped with an energy dispersive QUANTAX X-Ray analyzer
135 (EDX) (Bruker, Czech Republic) for chemical analysis. Elemental identification and quantitative
136 compositional analysis were performed by XRF and, in some cases, were supported by SEM-EDX.
137 The analysis of total Fe oxides in the sample was made by XRF. The mineralogical characterization
138 of the powdered samples was performed by X-ray diffraction analysis (XRD) using a Panalytical
139 diffractometer (Almelo, the Netherlands) and Cu K α radiation. The XRD interpretation software
140 was PDF-2 (Powdered Diffraction File-2) from the International Centre for Diffraction Data.

141 **2.2.2. Fourier transformation infrared spectroscopy**

142 FTIR spectra were recorded with an IRAffinity-1 Fourier transformation infrared
143 spectrophotometer (Shimadzu, Japan), equipped with a deuterated-triglycine sulfate (DTGS)
144 detector using a wavelength between 400 – 7000 cm⁻¹. Prior to being analyzed with FTIR, the
145 samples were transformed into pellets (diameter 7 mm) by using potassium bromide (KBr). This
146 method exploits the property that alkali halides (e.g. KBr) become plastic when subjected to
147 pressure and form a sheet that is transparent in the infrared region. KBr does not contain bands in
148 the mid-IR region of the spectrum and, therefore, the preparation as halide disks allows to lose less
149 information. FTIR was used to obtain a rapid and useful identification of Fe(III) precipitates and
150 information about the extent of metal substitution (Gotic and Music, 2007). Furthermore, with FTIR
151 spectroscopy, information about the adsorbed molecules and the nature of surface complexes could
152 be obtained (Cornell and Schwertmann, 2003).

153 **2.2.3. Raman spectroscopy**

154 Raman measurements were carried out with an INVIA spectrometer (Renishaw, United
155 Kingdom) equipped with a microscope and a charge coupled device (CCD) detector. A 532 nm

156 solid-state green (Nd:YAG) laser was used with a maximum power of 5 mW. The acquisitions were
157 performed through a x50 magnification objective (Leica, Germany) after achieving a calibration on
158 a silicon standard. The Rayleigh scattering component was removed by an Edge filter, and the
159 Raman-scattered light was dispersed by a holographic grating with 1800 lines/mm. The integration
160 time was set at 60 s. Specific preparation of the sample was not required. The theoretical spot size
161 was below 1 micrometer. Several spots on each sample were measured to avoid the measurement of
162 a small impurity instead of the main mineral.

163 **2.2.4. Thermal post-treatment**

164 A thermal post-treatment in a furnace at 650°C for 2 h was performed for some of the
165 samples to favor the crystallization of amorphous phases (calcination). The weight loss was
166 calculated according to (Eq. 1):

$$167 \quad \text{Weight Loss (\%)} = \frac{\text{weight}(25\text{ }^\circ\text{C}) - \text{weight}(650\text{ }^\circ\text{C})}{\text{weight}(25\text{ }^\circ\text{C})} \times 100 \quad (\text{Eq. 1})$$

168 The calcined products were characterized by XRD analysis.

169

170 **3. Results and Discussion**

171 **3.1. Effect of the activity of Fe(II)-oxidizing denitrifying bacteria on the mineralogy of** 172 **precipitates**

173 Table 1 reports the color, FTIR/Raman bands and the most intense XRD peaks (in inter-
174 reticular spacings) of the minerals observed in this study. The FTIR, Raman and XRD peaks/bands
175 were similar, indicating that the medium composition and the incubation conditions were likely

176 important factors for the Fe(III) (hydr)oxides formation. Many impurities and different minerals
177 apart from Fe(III) (hydr)oxides were present in all precipitates.

178 Raman spectroscopy is an easy and fast method for the identification of iron oxides, but also
179 different iron hydroxides and iron oxyhydroxides especially in poorly crystallized materials, which
180 are often formed in bioprocesses (Hanesch, 2009). None of the samples observed with the
181 microscope equipped in the Raman spectroscopy was homogeneous. A mixture of several spots
182 (dark, white, red and orange) in microscale was observed (Fig. 1). The differences in color
183 corresponded to different minerals. The single spot size for the measurement was approximately 1
184 μm , and several spots on each sample were measured to better characterize the entire Fe(III)
185 (hydr)oxides. Raman spectra of some characteristic bands are shown in Fig. 2. Some spectra also
186 showed a band at around 150-200 cm^{-1} (Fig. 2B). Fig. 2A shows a typical 2-line ferrihydrite
187 (Hanesch, 2009) of a dark spot in the sample PGN.

188 SEM inspection showed varying sizes and diverse geometrical shapes such as irregular, rod,
189 modular and spherical in diameter ranging from few nanometers to 15 μm (Fig. 3). Similarly,
190 Kappler and Newman (2004) found that Fe(III) precipitates, from bottles inoculated with the *R.*
191 *ferrooxidans* strain SW2, showed a variety of particles in the range of hundreds of nm to 20 μm .
192 These particles showed various shapes, e.g. needles and plates, as well as irregular shapes, as also
193 reported by Kappler et al. (2005). Fig. 3C, D shows the crystalline phases of the biogenic Fe(III)-
194 hydroxides obtained with the two pure cultures of *T. denitrificans* and *Pseudogulbenkiania* sp. 2002.
195 The biogenic minerals were in close association with the bacterial cell, forming a common globular
196 shape of biogenic minerals known as cell–mineral aggregate (Fig. 3C, D, Fig. 4B, C) (Schaedler et
197 al., 2009; Posth et al., 2014; Schmid et al., 2014). In comparison with the mixed cultures, the use of
198 pure cultures resulted in a higher amount of cell-mineral aggregates (Fig. 3).

199 All Raman spectra showed a band at around 1000 cm^{-1} , most likely indicating the presence
200 of siderite, i.e. an iron carbonate mineral (FeCO_3) (Fig. 2B, C) in agreement with the observations of
201 SEM-EDX analysis of some precipitates and the prediction of Visual MINTEQ reported by Kiskira
202 et al. (2018). Siderite spectra consisted of bands at 184, 287, 731 and 1090 cm^{-1} (Rull et al., 2004),
203 with the most common band being at 1090 cm^{-1} . The characteristic peak of siderite at $32.2^\circ 2\theta$ was
204 not observed by XRD analysis, as it likely overlapped with the hematite peak at $33.2^\circ 2\theta$ or the
205 siderite amount was not sufficient to be detected by XRD. Amounts of phosphate and carbonate
206 minerals were recorded by SEM-EDX. XRD and SEM analyses revealed the presence of vivianite,
207 i.e. $\text{Fe}_3(\text{PO}_4)_2 \cdot 8\text{H}_2\text{O}$, in many experiments with microorganisms (Fig. 3A, 5, Table 1). Similar to this
208 study, the use of the *Acidovorax* strain BoFeN1 in the presence of Fe(II) and acetate resulted in a
209 mixture of Fe(III) (hydr)oxides, vivianite and amorphous Fe(III)-phosphate as reported by Miot et
210 al. (2009) and Schaedler et al. (2009).

211 Ferrihydrite was most probably contained in all the samples, in agreement with the majority
212 of studies on nitrate-dependent ferrous oxidation (Straub et al., 1996, 2004; Hafenbradl et al., 1996;
213 Lack et al., 2002; Senko et al., 2005 a, b; Hohmann et al., 2009; Chakraborty et al., 2011; Zhao et
214 al., 2013; Miot et al., 2014; Li et al., 2014). FTIR was not a suitable method for the identification of
215 ferrihydrite precipitates that are impure and poorly crystallized (2-line ferrihydrite). The Mössbauer
216 spectroscopy might have supported a better characterization of such precipitates (Cornell and
217 Schwertmann, 2003). However, poorly crystalline phases in aqueous solution have been reported to
218 transform into goethite, hematite, lepidocrocite and other crystalline forms depending on the pH and
219 solution chemistry (Cornell and Schwertmann, 2003; Kappler and Newman, 2004). The
220 transformation of poorly crystalline Fe(III) into more crystalline phases requires atomic
221 reorganization, dissolution and re-precipitation (Kappler and Newman, 2004). The process can be

222 catalyzed by reducing agents such as cysteine or Fe(II) (Cornell and Schwertmann, 2003). The
223 presence of reducing agents or Fe(II) in combination with surface bridging ligands can induce a
224 reductive dissolution of poorly crystalline Fe(III)-oxides and the subsequent re-precipitation of more
225 highly ordered phases (Cornell et al., 1989; Kappler and Newman, 2004). This stands in line with
226 this study, with ferrihydrite being always present with other more crystalline phases (Fig. 3A, Table
227 1). The transformation of the initial precipitates into more crystalline phases is generally faster in the
228 presence of bacteria, through acidification of the local environment followed by an acid-catalyzed
229 dissolution of Fe(III)-minerals or a reduction of Fe(III) (Kappler and Newman, 2004).

230 In this study, the mineralogy of the precipitates was only analyzed at the end of the
231 experiments, and no additional information can be given on the production rate of the minerals in
232 the presence of microorganisms. In terms of nitrate removal and Fe(II) oxidation, Kiskira et al.
233 (2018) observed the highest specific rates with the *Thiobacillus*-dominated mixed culture, while the
234 lowest specific rates were obtained in the bioassays with the *Pseudogulbenkiania* sp. 2002. A higher
235 Fe(II) oxidation rate has been related to the formation of less crystallized phases, while a lower
236 Fe(II) oxidation rate produces crystalline minerals (Lack et al., 2002; Senko et al., 2005b). However,
237 the effect of the reaction rate needs further investigation due to a mixture of Fe(III) (hydr)oxides of
238 amorphous phase, poorly crystalline and crystalline phases that are generally produced
239 simultaneously.

240 Table 2 reports the amount (%) of Fe oxides in each sample obtained in this study. The use
241 of the *Thiobacillus*-mixed culture resulted in 61% of Fe(III) oxides in the corresponding precipitate.
242 A slightly lower percentage of 57 and 55% was observed when the pure *T. denitrificans* culture and
243 the activated sludge enrichment were used, respectively. The use of *Pseudogulbenkiania* strain 2002
244 resulted in 50% of Fe(III) oxides in the precipitate. An eye-catching color method was also used for

245 an easy and fast identification of the iron oxides (Cornell and Schwertmann, 2003). However,
246 Fe(III) precipitates consisted of a mixture of (hydr)oxides with many impurities and the color
247 identification was, thus, not reliable. When transformed into a powder, the precipitates showed a
248 different color, which is reported in Table 1.

249 When the activated sludge enrichment was used, the liquid phase turned into a reddish and
250 brownish color throughout the experiments (Fig. S1). In the bottles with the *Thiobacillus*-mixed
251 culture, the color was more red than brown. The pure *T. denitrificans* and *Pseudogulbenkiania* strain
252 2002 resulted in a darker reddish brown or even black color (Fig. S1). Other studies observed a
253 white fluffy structure that turned into a greenish/gray or reddish/orange substance within a week
254 after the start of the incubation (Chaudhuri et al., 2001; Miot et al., 2009; Pantke et al., 2012). Green
255 rusts as major products cause a grayish/green appearance (Straub et al., 1996) and Fe(III)
256 oxyhydroxide or ferrihydrite generally give an orange/brown color to the liquid phase (Lack et al.,
257 2002), as also observed in this study.

258 3.1.1. *Thiobacillus*-mixed (TM) culture

259 The precipitates of the experiments carried out with the *Thiobacillus*-dominated mixed
260 culture were a mixture of hematite, akaganeite and/or ferrihydrite. The infrared spectrum of the
261 precipitates with the *Thiobacillus*-mixed culture showed strong bands at 540 and 3380 cm⁻¹ (Fig.
262 S2A, Table 1), which are typical of hematite (Cornell and Schwertmann, 2003). Hematite was also
263 detected with Raman spectroscopy and XRD. In the dark spots having a diameter of approximately
264 2.5 μm, the combination of bands at 225, 290-300 and 412 cm⁻¹ was observed (Table 1, Fig. S3A),
265 as well as a typical peak at around 24°2θ in the XRD spectrum (Fig. 5A).

266 Strong bands at 1630 and 1050 cm⁻¹ in the infrared spectrum (S2A, Table 1) most likely
267 corresponded to akaganeite, as confirmed by the two broad bands at 700 and 400 cm⁻¹ obtained for

268 the red spots in Raman spectra (diameter 3 μm) (Fig. S3B) (Boucherit et al., 1989). However, the
269 band at around 700 cm^{-1} might also have been due to ferrihydrite. In six-line ferrihydrite, three bands
270 at 370, 510 and 710 cm^{-1} , while in two-line ferrihydrite only the strong 710 cm^{-1} band can be seen
271 (Mazzetti and Thistlethwaite, 2002). However, none of the FTIR bands of ferrihydrite at 3615, 3430,
272 650, 450 cm^{-1} was observed in the infrared spectrum, indicating that the red spots probably
273 corresponded to akaganeite. No XRD peak of akaganeite at $11.9^\circ 2\theta$ was observed, presumably due
274 to overlapping with the peak of vivianite at $11.2^\circ 2\theta$ (Cornell and Schwertmann, 2003), in agreement
275 with SEM observations that showed the presence of vivianite.

276 The formation of akaganeite was likely stimulated by the presence of chloride ions. The
277 structural network of akaganeite consists of tunnels with large cavities surrounded by double rows
278 of edge-shared octahedral with Fe^{3+} , Cl^- or H_2O molecules. The structure has two double chains that
279 are corner-shared to neighboring double chains, forming a 3D network that differs from all other
280 Fe(III) hydr(oxides) (body-centered cubic array) and stabilizes the tunnel structure of $\beta\text{-FeOOH}$
281 crystals (Cornell and Schwertmann, 2003; dos Santos et al., 2016).

282 **3.1.2. *T. denitrificans* (TDP) pure culture**

283 When the pure culture of *T. denitrificans* was used, maghemite was observed on top of
284 hematite and/or ferrihydrite (Table 1). Raman spectra of the red spots (diameter $\sim 5 \mu\text{m}$) identified
285 bands at 350, 700, 1300 and 1600 cm^{-1} that corresponded to maghemite (Fig. S3D, Table 1)
286 (Hanesch, 2009). No other maghemite bands at 512 and 664 cm^{-1} were identified, in contrast to what
287 was reported by Jacintho et al. (2007). The FTIR, Raman and XRD analyses confirmed also the
288 presence of hematite. Raman spectra of the dark spots showed bands at 225, 290-300, 412 and,
289 additionally, 611 cm^{-1} , all corresponding to hematite (Fig. S3C). The band at 700 cm^{-1} could also be
290 ascribed to the presence of two-line ferrihydrite. The additional FTIR bands at 1400 and 2360 cm^{-1}

291 were impurities (Fig. S2D), probably due to the presence of nitrate (Cornell and Schwertmann,
292 2003).

293 **3.1.3. Activated sludge (AS) enrichment**

294 The activated sludge enrichment allowed the production of hematite and maghemite and/or
295 magnetite (and/or ferrihydrite). The FTIR spectrum showed bands as TDP and TM cultures (Fig.
296 S2B), and Raman spectra as well as XRD (2θ) confirmed the presence of hematite (Table 1, Fig.
297 5B). Similarly, Sun et al. (2009) reported the formation of a mixture of Fe(III) oxides dominated by
298 crystalline hematite with the use of a sludge inoculum in a lab-scale As(III)-oxidizing denitrifying
299 bioreactor.

300 The Raman bands at 1300 and 1600 cm^{-1} in dark and red spots likely corresponded to
301 maghemite and/or magnetite (Fig. 2C). The Raman spectrum of white spots showed bands at 350,
302 500, 700 and 1350 cm^{-1} , very similar to the maghemite bands at 350, 512, 664, 726 and 1330 cm^{-1}
303 reported by Hanesch (2009). However, the FTIR bands at 3740 and 3725 cm^{-1} corresponding to the
304 OH groups of maghemite were not recorded, indicating that the spectrum was likely a mixture of
305 magnetite and maghemite (Busca et al., 1993). De Faria et al. (1997) reported three Raman broad
306 peaks at 350, 500 and 700 cm^{-1} in the maghemite spectrum. The Raman broad band from 653 to 750
307 cm^{-1} that can be observed in all samples can be caused by magnetite and maghemite (Hanesch et al.,
308 2009). Raman bands of magnetite were observed at 309 and 540 cm^{-1} , whereas maghemite peaks at
309 344 and 490 cm^{-1} (Table 1). The Raman band above 1300 cm^{-1} of maghemite was relatively weak
310 compared to the other bands, probably due to the presence of magnetite. The red spots might also
311 have contained six-line or two-line ferrihydrite, corresponding to the three bands observed at 350,
312 500 and 700 cm^{-1} .

313 **3.1.4. *Pseudogulbenkiania* (PG) strain 2002**

314 The use of the pure culture of *Pseudogulbenkiania* strain 2002 resulted in hematite and
315 maghemite formation (and/or ferrihydrite). FTIR spectra showed the bands of hematite (Fig. S2C),
316 such as the Raman spectra with the additional band at 1600 cm^{-1} corresponding to maghemite (Fig.
317 2B, Table 1). Zhao et al. (2013) reported that *Pseudogulbenkiania* strain 2002 allowed the formation
318 of vivianite, ferrihydrite and magnetite. Xiu et al. (2016) used *Pseudogulbenkiania* strain 2002 and
319 reported that lepidocrocite was the only crystalline biogenic solid formed. In this study, only
320 amorphous phases were reported by XRD analyses and similar to those obtained with the activated
321 sludge enrichment (Fig. 5B, Table 1). Crystalline phases were observed by SEM, although it was not
322 possible to distinguish between the different hydr(oxides) (Fig. 2C).

323 **3.2. Precipitates in abiotic controls**

324 Chemical Fe(II) oxidation mainly resulted in the formation of hematite and another mineral
325 between goethite or akaganeite. Also, a well crystallized vivianite ($\text{Fe}_3(\text{PO}_4)_2 \cdot 8\text{H}_2\text{O}$) in the typical
326 monoclinic crystal system and siderite (FeCO_3) were easily identified by EDX (Fig. 3A and 4A).
327 White, grey and reddish precipitates were observed in abiotic controls in the first 24 hours. In
328 agreement, white precipitates from chemical Fe(II) oxidation in both biotic and abiotic experiments
329 were reported elsewhere (Miot et al., 2009).

330 The infrared spectrum of the precipitates in the abiotic controls (AC) showed strong bands at
331 470 and 3380 cm^{-1} , which are typical of hematite (Fig. 6). The band at 3380 cm^{-1} most likely
332 corresponded to the hydroxyl groups in the hematite crystals (Rochester and Topham, 1979). The
333 presence of hematite was also confirmed by the reddish color of the AC sample (Table 1).

334 The obtained particles were aggregates of larger globular shaped particles than those
335 obtained in experiments with microorganisms (Fig. 3). Dark and red spots (diameter $\sim 10\text{ }\mu\text{m}$) were
336 observed with the microscope equipped in the Raman spectrometer. The Raman spectra of the dark

337 spots showed bands at 225, 290-300, 412 and 611 cm^{-1} , which permitted to identify hematite (Table
338 1) (Oh et al., 1998) as also confirmed by FTIR analysis (Fig. 6). Furthermore, a band at 1321 cm^{-1} ,
339 corresponding to hematite, was also observed due to the presence of red spots.

340 The FTIR band at 1630 cm^{-1} was probably related to the position of H_2O bending vibrations
341 of goethite or the presence of the typical O-H bending of akaganeite, whereas the band at 1050 cm^{-1}
342 could be ascribed to a significant amount of adsorbed impurities in goethite particles (Gotic and
343 Music, 2007) (Table 1). Chemical Fe(II) oxidation results in the formation of goethite (Park et al.,
344 2014), also in the presence of high concentrations of HCO_3^- (Larese-Casanova et al., 2010).
345 However, the band at 1630 cm^{-1} can also be related to the formation of akaganeite, and the
346 additional band observed at 1050 cm^{-1} has been reported in akaganeite samples in KBr discs, which
347 were considered to be artefacts (Murad and Bishop, 2000). However, no goethite or akaganeite
348 bands were observed in Raman spectra.

349 **3.3. Mineralogy of the precipitates in the presence of metals**

350 Copper, nickel and zinc have been reported to be essential for the structure of several
351 precipitates, such as akaganeite and maghemite (Deliyanni et al. 2007; Drogenik et al., 2008; Nador
352 et al, 2013; dos Santos et al., 2016; Hu et al., 2016; Suzuki et al., 2017). However, no previous
353 studies have investigated the effects of these metals on the formation of biogenic minerals by
354 nitrate-dependent Fe(II)-oxidizing microorganisms. In this study, all the precipitates contained Cu,
355 Ni, Zn, indicating metal precipitation, co-precipitation and sorption onto iron (hydr)oxides (Table
356 2). This is in agreement with the decrease of the soluble Cu, Ni and Zn concentration and the
357 prediction of Visual MINTEQ reported by Kiskira et al. (2018).

358 The addition of Cu resulted in a red to brown liquid phase and a browner liquid phase was
359 observed with the addition of Ni and Zn. The elemental identification and quantitative

360 compositional analysis performed by XRF and SEM-EDX of the precipitates obtained with the three
361 heavy metals are shown in Table 2. When Cu was supplemented, a higher amount of Fe(III) oxides
362 by 20 and 15% was obtained with the pure cultures of *T. denitrificans* and *Pseudogulbenkiania*
363 strain 2002, respectively, compared to the precipitates obtained from the bottles without metals. In
364 contrast, a decrease by 14 and 13% was observed in the samples with the *Thiobacillus*-mixed culture
365 and activated sludge enrichment (Table 2). The addition of Ni resulted in an increase of the Fe(III)
366 oxides formation in the range of 5-20% with all the microbial cultures. The precipitates obtained in
367 the presence of Zn had a lower amount of Fe oxides by 6 and 2% with the *Thiobacillus*-mixed
368 culture and the *Pseudogulbenkiania* strain 2002, respectively, whereas an increase by 22 and 9%
369 was observed in bottles with activated sludge and the *T. denitrificans* pure culture (Table 2).

370 The addition of metal salts such as Ni, Cu and Zn likely prevented the crystallization of
371 vivianite, thus determining the prevalent formation of amorphous phases (Fig. 5C, D). Hematite and
372 $K_2CaP_2O_7$ have been detected in ASC and TMC samples by XRD, respectively (Table 1). With all
373 the techniques used, the presence of Cu, Ni and Zn resulted in similar Fe(III) (hydr)oxide
374 precipitates as those obtained in the absence of metals, probably due to their low concentrations
375 (Table 1). No significant differences by SEM were observed with the addition of metals (Cu, Ni,
376 Zn), except the formation of covellite (CuS) in the experiments with the activated sludge enrichment
377 and the addition of Cu (Fig. 4E). Traces of sulfate were present in the basal medium, and covellite
378 was formed likely due to the sulfidogenic activity of sulfate reducing bacteria present in the
379 activated sludge enrichment (Gramp et al., 2006; Villa-Gomez et al., 2012; Papirio et al., 2013). No
380 significant differences were observed between the PG and PGC samples with *Pseudogulbenkiania*
381 sp. 2002.

382 Using all the microbial cultures, the mineralogy of the precipitates was not considerably
383 affected by the presence of Cu (Table 1). The precipitates obtained with the *Thiobacillus*-mixed
384 culture in the presence of Cu (TMC) were most likely a mixture of akaganeite and hematite, as also
385 observed in the TM precipitates. The addition of Cu resulted in a broad band at 3448 cm⁻¹, likely
386 corresponding to the 3480+3390 (doublet) (OH and H₂O stretch) of akaganeite, as also confirmed by
387 the additional band at around 500 cm⁻¹ that was due to the Fe-O stretch of akaganeite (Table 1). The
388 strong band at 3448 cm⁻¹ might also be ascribed to the surface hydroxyl groups of goethite (Cornell
389 and Schwertmann, 2003). However, the intense band of hydroxyl stretch of goethite at 3140 cm⁻¹
390 and the typical band at 3666 cm⁻¹ were not observed, most likely due to the presence of phosphate in
391 the medium as reported by Russell et al. (1979).

392 When the *T. denitrificans* pure culture was used, another band of hematite at 470 instead of
393 540 cm⁻¹ was recorded in the TDPC sample (Table 1). The Raman bands at 225, 412 and 1321 cm⁻¹
394 corresponded to hematite and an additional band at 700 cm⁻¹ probably indicated the presence of two-
395 line ferrihydrite. The bands at 700 and 1330 cm⁻¹ were likely due to maghemite, in agreement with
396 what was observed in the TDP sample. Similarly, the ASC sample collected from the bottle seeded
397 with the activated sludge enrichment in the presence of Cu showed the same FTIR bands as for
398 TMC. Hematite, maghemite and/or magnetite and/or two-line ferrihydrite were identified from the
399 Raman spectra (Table 1). However, SEM micrographs of samples from experiments using the
400 activated sludge enrichment with addition of Cu mostly showed amorphous phases (Fig. 4D).

401 The addition of Ni led to more significant differences in the mineralogy of the precipitates
402 obtained with the four microbial cultures. The infrared spectrum of the precipitate obtained with the
403 *Thiobacillus*-mixed culture in the presence of Ni (TMN) showed some additional FTIR peaks at
404 3430, 940, 650 and 450 cm⁻¹, corresponding to bulk OH deformations and stretch of ferrihydrite

405 (Table 1). The band revealed at 940 cm^{-1} has already been reported when ferrihydrite contains a few
406 percent of Si (Schwertmann and Thalmann, 1976). In this study, the presence of Si was confirmed by
407 the XRF analysis (Table 2). A strong band at 1630 cm^{-1} likely indicated the presence of akaganeite.
408 Hematite was revealed by the Raman spectrum of the dark spots (Fig. 3). The additional broad band
409 of maghemite at about 1300 cm^{-1} was observed, indicating that the addition of Ni might stimulate
410 the formation of maghemite (Table 1), also in the *T. denitrificans* (TDPN), activated sludge
411 enrichment (ASN) and *Pseudogulbenkiania* strain 2002 (PGN) samples. In contrast to other studies
412 on denitrification in the presence of Ni (Zou et al., 2015), no specific Ni precipitate, such as
413 $\text{Ni}_3(\text{PO}_4)_2$, was observed with XRD likely due to the lower Ni concentrations used.

414 The FTIR spectrum of the precipitates taken from the bottles inoculated with *Thiobacillus*-
415 mixed culture in the presence of Zn (TMZ) showed a mixture of ferrihydrite and akaganeite (Table
416 1). The FTIR band at 3430 cm^{-1} and the broad band at 940 cm^{-1} of ferrihydrite were observed, as
417 well as the bands at 1630 , 410 and 1050 cm^{-1} corresponding to akaganeite (Table 1). An additional
418 band at 1384 cm^{-1} might be associated with nitrate in ferrihydrite (Cornell and Schwertmann, 2003).
419 Differently to other samples, orange spots were observed by Raman spectroscopy and likely
420 corresponded to hematite, as hematite peaks at 225 , 245 , 411 and 1321 cm^{-1} were visible. The bands
421 of TDPZ, ASZ and PGZ are reported in Table 1. The FTIR and Raman spectra were similar to those
422 obtained with the addition of Ni for all microbial cultures, indicating that also the presence of Zn
423 likely stimulated the formation of maghemite. XRD analysis of ASZ indicated the possible presence
424 of maghemite with the peak at $35^\circ 2\theta$.

425 **3.4. Thermal post-treatment**

426 The goal of the thermal post-treatment of mineral phases is of double interest. Firstly, it
427 allows to evaluate the weight loss due to desorption and decomposition phenomena of the phases

428 present in the products. Strong endothermic effects are mainly related to the water loss, due to the
429 adsorption and crystallization as well as the reaction of decomposition of hydroxides, oxy-
430 hydroxides and nitrate among others. Secondly, it is possible to assess the potential for
431 crystallization of the amorphous phases.

432 To this end, the precipitates were thermally treated at 650°C for 2 h and the products were
433 characterized by XRD analysis (Table 1) and weight loss (Eq. 1) due to calcination. The thermal
434 treatment improved the crystallinity of hematite and favored the formation of some other crystalline
435 phases with P in abiotic controls (Table 1). Similarly, the thermal treatment favored the formation of
436 hematite in all samples (Fig. 7) and crystalline phases of Fe with P and Na, due to their high P
437 content, i.e. FePO_4 , $\text{Fe}_2(\text{III})\text{Fe}(\text{II})(\text{P}_2\text{O}_7)_2$ and NaFePO_4 , in TM and AS samples (Table 1, Fig. 7).

438 According to the chemical analysis, the NaFePO_4 phase appears to crystallize when the
439 amount of Na is higher than Cl. In this case and at low P content, the crystalline NaFeO_2 was
440 detected in the ASC sample (Table 1). When the amount of Na was lower than Ca and the P content
441 was relatively high, the crystalline $\text{Fe}_2(\text{III})\text{Fe}(\text{II})(\text{P}_2\text{O}_7)_2$ was formed (AS and AC samples).

442 The weight loss for some samples was also determined (Table 3) and ranged between 24.4
443 and 61.9%. The thermal treatment allows the generation of samples with a different volumetric bulk.
444 Samples with a higher weight loss have a higher volumetric bulk compared with those having a
445 lower volume. In a comparison between the samples obtained with the different Fe(II)-oxidizing
446 denitrifying microorganisms, the use of *Pseudogulbenkiania* strain 2002 (PG, PGC, PGN and PGZ
447 samples) resulted in a higher weight loss due to the higher amount of biomass and higher amount of
448 water stored, likely indicating that the post-treatment requires a higher energy consumption
449 necessary for iron recovery.

450

451 **4. Conclusions**

452 Fe(II)-mediated autotrophic denitrification resulted in the formation of a mixture of
453 amorphous phase or poorly crystalline Fe(III) (hydr)oxides (e.g. ferrihydrite), but also in some
454 crystalline phases such as hematite, akaganeite and maghemite. The use of the *Thiobacillus*-
455 dominated mixed culture mainly led to the formation of akaganeite. Maghemite was more
456 intensively observed when the activated sludge enrichment and the two pure cultures of *T.*
457 *denitrificans* and *Pseudogulbenkiania* strain 2002 were used. The thermal post-treatment showed
458 that the experiments generated iron oxide precipitates with different volumetric bulk. The use of
459 *Pseudogulbenkiania* strain 2002 resulted in an almost double weight loss of the precipitates,
460 inducing a higher energy consumption necessary for iron recovery. Cu, Ni and Zn were identified in
461 the precipitates by chemical analyses, indicating that metal precipitation, co-precipitation or sorption
462 onto iron (hydr)oxides occurred. However, no difference in the mineralogy of the iron precipitates
463 was observed with the addition of Cu, whereas the addition of Ni and Zn stimulated the formation of
464 maghemite.

465

466 **Acknowledgments**

467 The study was carried out in the framework of the Erasmus Mundus Joint Doctorate ETeCoS³
468 (Environmental Technologies for Contaminated Solids, Soils, and Sediments) funded by the
469 European Commission under the grant agreement FPA n°2010-0009. Kyriaki Kiskira was supported
470 by a grant from the Italian Ministry of Education, University and Research (MIUR).

471

472

473 **References**

- 474 1. Ahoranta, S.H., Kokko, M.E., Papirio, S., Özkaya, B. and Puhakka, J.A., (2016). Arsenic
475 removal from acidic solutions with biogenic ferric precipitates, *Journal of Hazardous*
476 *Materials*, 306, pp. 124-132.
- 477 2. Boucherit, N., Delichere, P., Joiret, S. and Hugot le Goff, A., (1989). Passivity of iron and
478 iron alloys studied by voltammetry and Raman spectroscopy, *In Materials Science Forum*,
479 44, pp. 51-62.
- 480 3. Busca, G., Lorenzelli, V., Ramis, G. and Willey, R.J., (1993). Surface sites on spinel-type
481 and corundum-type metal oxide powders, *Langmuir*, 9, pp. 1492-1499.
- 482 4. Chakraborty, A., Roden, E.E., Schieber, J. and Picardal, F., (2011). Enhanced growth of
483 *Acidovorax* sp. strain 2AN during nitrate-dependent Fe (II) oxidation in batch and
484 continuous-flow systems, *Applied and Environmental Microbiology*, 77, pp. 8548-8556.
- 485 5. Cornell, R.M., Schneider, W. and Giovanoli, R., (1989). The transformation of ferrihydrite
486 into lepidocrocite, *Clay Minerals*, 24, pp. 549-553.
- 487 6. Cornell, R. and Schwertmann, U., (2003). *The Iron Oxides: Structures, Properties,*
488 *Reactions, Occurrences and Uses*. 2nd ed. Weinheim: Wiley-VCH, pp. 345-363, 509-524.
- 489 7. dos Santos, P.L., Guimarães, I.R., Mesquita, A.M. and Guerreiro, M.C., (2016). Copper-
490 doped akaganeite: Application in catalytic Cupro-Fenton reactions for oxidation of
491 methylene blue, *Journal of Molecular Catalysis A: Chemical*, 424, pp. 194-202.
- 492 8. Cao, Z., Qin, M., Jia, B., Gu, Y., Chen, P., Volinsky, A.A. and Qu, X., (2015). One pot
493 solution combustion synthesis of highly mesoporous hematite for photocatalysis, *Ceramics*
494 *International*, 41, pp. 2806-2812.

- 495 9. Chaudhuri, S.K., Lack, J.G. and Coates, J.D., (2001). Biogenic magnetite formation through
496 anaerobic biooxidation of Fe(II), *Applied and Environmental Microbiology*, 67, pp. 2844-
497 2848.
- 498 10. Chen, A., Shang, C., Shao, J., Zhang, J. and Huang, H., (2017). The application of iron-
499 based technologies in uranium remediation: A review, *Science of the Total Environment*,
500 575, pp. 1291-1306.
- 501 11. De Faria, D.L.A., Venâncio Silva, S. and De Oliveira, M.T., (1997). Raman
502 microspectroscopy of some iron oxides and oxyhydroxides, *Journal of Raman spectroscopy*,
503 28, pp. 873-878.
- 504 12. Deliyanni, E.A., Peleka, E.N. and Matis, K.A., (2007). Removal of zinc ion from water by
505 sorption onto iron-based nanoadsorbent, *Journal of hazardous materials*, 141, pp. 176-184.
- 506 13. Di Capua, F., Ahoranta, S.H., Papirio, S., Lens, P.N.L. and Esposito G., (2016). Impacts of
507 sulfur source and temperature on sulfur-driven denitrification by pure and mixed cultures of
508 *Thiobacillus*, *Process Biochemistry*, 51, pp. 1576-1584.
- 509 14. Drogenik, M., Kristl, M., Makovec, D., Jagličić, Z. and Hanžel, D., (2008). Sonochemically
510 assisted synthesis of zinc-doped maghemite, *Ultrasonics Sonochemistry*, 15, pp. 791-798.
- 511 15. Fajardo, C., Costa, G., Nande, M., Martín, C., Martín, M. and Sánchez-Fortún, S., (2019).
512 Heavy metals immobilization capability of two iron-based nanoparticles (nZVI and Fe₃O₄):
513 Soil and freshwater bioassays to assess ecotoxicological impact, *Science of The Total*
514 *Environment*, 656, pp. 421-432.
- 515 16. Gotic, M. and Music, S., (2007). Mössbauer, FT-IR and FE SEM investigation of iron oxides
516 precipitated from FeSO₄ solutions, *Journal of Molecular Structure*, 834, pp.445-453.

- 517 17. Gramp, J.P., Sasaki, K., Bigham, J.M., Karnachuk, O.V. and Tuovinen, O.H., (2006).
518 Formation of covellite (CuS) under biological sulfate-reducing conditions, *Geomicrobiology*
519 *Journal*, 23, pp. 613-619.
- 520 18. Hafenbradl, D., Keller, M., Dirmeier, R., Rachel, R., Roßnagel, P., Burggraf, S., Huber, H.
521 and Stetter, K.O., (1996). *Ferroglobus placidus* gen. nov., sp. nov., a novel
522 hyperthermophilic archaeum that oxidizes Fe²⁺ at neutral pH under anoxic conditions,
523 *Archives of Microbiology*, 166, pp. 308-314.
- 524 19. Hanesch, M., (2009). Raman spectroscopy of iron oxides and (oxy) hydroxides at low laser
525 power and possible applications in environmental magnetic studies, *Geophysical Journal*
526 *International*, 177, pp. 941-948.
- 527 20. Hennebel, T., De Gusseme, B., Boon, N. and Verstraete, W., (2009). Biogenic metals in
528 advanced water treatment, *Trends in Biotechnology*, 27, pp. 90-98.
- 529 21. Hohmann, C., Winkler, E., Morin, G. and Kappler, A., (2009). Anaerobic Fe (II)-oxidizing
530 bacteria show As resistance and immobilize As during Fe (III) mineral precipitation,
531 *Environmental Science & Technology*, 44, pp. 94-101.
- 532 22. Hu, J., Chen, G. and Lo, I.M., (2006). Selective removal of heavy metals from industrial
533 wastewater using maghemite nanoparticle: performance and mechanisms, *Journal of*
534 *Environmental Engineering*, 132, pp. 709-715.
- 535 23. Jacintho, G.V., Corio, P. and Rubim, J.C., (2007). Surface-enhanced Raman spectra of
536 magnetic nanoparticles adsorbed on a silver electrode, *Journal of Electroanalytical*
537 *Chemistry*, 603, pp. 27-34.
- 538 24. Kappler, A. and Newman, D.K., (2004). Formation of Fe (III)-minerals by Fe (II)-oxidizing
539 photoautotrophic bacteria, *Geochimica et Cosmochimica Acta*, 68, pp. 1217-1226.

- 540 25. Kappler, A. and Straub, K.L., (2005). Geomicrobiological cycling of iron, *Reviews in*
541 *Mineralogy & Geochemistry*, 59, pp. 85-108.
- 542 26. Kappler, A., Schink, B. and Newman, D.K., (2005). Fe (III) mineral formation and cell
543 encrustation by the nitrate-dependent Fe (II)-oxidizer strain BoFeN1, *Geobiology*, 3, pp.
544 235-245.
- 545 27. Kiskira, K., Papirio, S., van Hullebusch, E.D. and Esposito, G., (2017a). Fe(II)-mediated
546 autotrophic denitrification: A new bioprocess for iron bioprecipitation/biorecovery and
547 simultaneous treatment of nitrate-containing wastewaters, *International Biodeterioration &*
548 *Biodegradation*, 119, pp. 631-648.
- 549 28. Kiskira, K., Papirio, S., van Hullebusch, E.D. and Esposito, G., (2017b). Influence of pH,
550 EDTA/Fe (II) ratio, and microbial culture on Fe (II)-mediated autotrophic denitrification,
551 *Environmental Science and Pollution Research*, 24, pp. 21323-21333.
- 552 29. Kiskira, K., Papirio, S., Fourdrin, C., van Hullebusch, E.D. and Esposito, G., (2018). Effect
553 of Cu, Ni and Zn on Fe(II)-driven autotrophic denitrification, *Journal of Environmental*
554 *Management*, 218, pp. 209-219.
- 555 30. Konhauser, K.O., Kappler, A. and Roden, E.E., (2011). Iron microbial metabolisms,
556 *Elements*, 7, pp. 89-93.
- 557 31. Lack, J.G, Chaudhuri, S.K., Kelly, S.D., Kemner, K.M., O'Connor, S.M. and Coates, J.D.,
558 (2002). Immobilization of radionuclides and heavy metals through anaerobic bio-oxidation
559 of Fe(II), *Applied and Environmental Microbiology*, 68, pp. 2704-2710.
- 560 32. Larese-Casanova, P., Haderlein, S.B. and Kappler, A., (2010). Biomineralization of
561 lepidocrocite and goethite by nitrate-reducing Fe(II)-oxidizing bacteria: Effect of pH,
562 bicarbonate, phosphate, and humic acids, *Geochimica et Cosmochimica Acta*, 74, pp. 3721-
563 3734.

- 564 33. Mazzetti, L. and Thistlethwaite, P.J., (2002). Raman spectra and thermal transformations of
565 ferrihydrite and schwertmannite, *Journal of Raman Spectroscopy*, 33, pp. 104-111.
- 566 34. Miot, J., Benzerara, K., Morin, G., Bernard, S., Beyssac, O., Larquet, E., Kappler, A. and
567 Guyot, F., (2009). Transformation of vivianite by anaerobic nitrate-reducing iron-oxidizing
568 bacteria, *Geobiology*, 7, pp. 373-384.
- 569 35. Miot, J., Li, J., Benzerara, K., Sougrati, M.T., Ona-Nguema, G., Bernard, S., Jumas, J.C. and
570 Guyot, F., (2014). Formation of single domain magnetite by green rust oxidation promoted
571 by microbial anaerobic nitrate-dependent iron oxidation, *Geochimica et Cosmochimica Acta*,
572 139, pp. 327-343.
- 573 36. Murad, E. and Bishop, J.L., (2000). The infrared spectrum of synthetic akaganéite, β -
574 FeOOH, *American Mineralogist*, 85, pp. 716-721.
- 575 37. Nador, F., Volpe, M.A., Alonso, F., Feldhoff, A., Kirschning, A. and Radivoy, G., (2013).
576 Copper nanoparticles supported on silica coated maghemite as versatile, magnetically
577 recoverable and reusable catalyst for alkyne coupling and cycloaddition reactions, *Applied*
578 *Catalysis A: General*, 455, pp. 39-45.
- 579 38. Nielsen, J.L. and Nielsen, P.H., (1998). Microbial nitrate-dependent oxidation of ferrous iron
580 in activated sludge, *Environmental Science & Technology*, 32, pp. 3556-3561.
- 581 39. Li, B., Tian, C., Zhang, D. and Pan, X., (2014). Anaerobic nitrate-dependent iron(II)
582 oxidation by a novel autotrophic bacterium, *Citrobacter freundii* Strain PXL1,
583 *Geomicrobiology Journal*, 31, pp. 138-144.
- 584 40. Oh, S.J., Cook, D.C. and Townsend, H.E., (1998). Characterization of iron oxides commonly
585 formed as corrosion products on steel, *Hyperfine Interact.*, 112, pp. 59-65.

- 586 41. Pantke, C., Obst, M., Benzerara, K., Morin, G., Ona-Nguema, G., Dippon, U. and Kappler,
587 A., (2012). Green rust formation during Fe (II) oxidation by the nitrate-reducing *Acidovorax*
588 sp. strain BoFeN1, *Environmental Science & Technology*, 46, pp. 1439-1446.
- 589 42. Papirio, S., Esposito, G. and Pirozzi, F., (2013). Biological inverse fluidized-bed reactors for
590 the treatment of low pH- and sulphate-containing wastewaters under different COD/SO₄²⁻
591 conditions. *Environmental Technology*, 34, pp. 1141-1149.
- 592 43. Papirio, S., Zou, G., Ylinen, A., Di Capua, F., Pirozzi, F. and Puhakka, J.A., (2014). Effect
593 of arsenic on nitrification of simulated mining water, *Bioresource Technology*, 164, pp. 149-
594 154.
- 595 44. Park, S., Kim, D.H., Lee, J.H. and Hur, H.G., (2014). *Sphaerotilus natans* encrusted with
596 nanoball-shaped Fe (III) oxide minerals formed by nitrate-reducing mixotrophic Fe (II)
597 oxidation, *FEMS Microbiology Ecology*, 90, pp. 68-77.
- 598 45. Pat-Espadas, A.M. and Cervantes, F.J., (2018). Microbial recovery of metallic nanoparticles
599 from industrial wastes and their environmental applications, *Journal of Chemical*
600 *Technology & Biotechnology*, 93, pp.3091-3112.
- 601 46. Pouran, S.R., Raman, A.A.A. and Daud, W.M.A.W., (2014). Review on the application of
602 modified iron oxides as heterogeneous catalysts in Fenton reactions, *Journal of Cleaner*
603 *Production*, 64, pp. 24-35.
- 604 47. Posth, N.R., Canfield, D.E. and Kappler, A., (2014). Biogenic Fe (III) minerals: from
605 formation to diagenesis and preservation in the rock record, *Earth-Science Reviews*, 135, pp.
606 103-121.
- 607 48. Rochester, C.H. and Topham, S.A., (1979). Infrared study of surface hydroxyl groups on
608 haematite, *Journal of the Chemical Society, Faraday Transactions 1: Physical Chemistry in*
609 *Condensed Phases*, 75, pp. 1073-1088.

- 610 49. Rull, F., Martinez-Frias, J., Sansano, A., Medina, J. and Edwards, H.G.M., (2004).
611 Comparative micro-Raman study of the Nakhla and Vaca Muerta meteorites, *Journal of*
612 *Raman Spectroscopy*, 35, pp. 497-503.
- 613 50. Russell, J. D., (1979). Infrared spectroscopy of ferrihydrite: evidence for the presence of
614 structural hydroxyl groups, *Clay Minerals*, 14, pp. 190-214.
- 615 51. Schaedler, S., Burkhardt, C., Hegler, F., Straub, K.L., Miot, J., Benzerara, K. and Kappler,
616 A., (2009). Formation of cell-iron-mineral aggregates by phototrophic and nitrate-reducing
617 anaerobic Fe(II)-oxidizing bacteria, *Geomicrobiology Journal*, 26, pp. 93-103.
- 618 52. Schmid, G., Zeitvogel, F., Hao, L., Ingino, P., Kuerner, W., Dynes, J.J., Karunakaran, C.,
619 Wang, J., Lu, Y., Ayers, T. and Schietinger, C., (2014). Synchrotron-based chemical nano-
620 tomography of microbial cell-mineral aggregates in their natural, hydrated state, *Microscopy*
621 *and Microanalysis*, 20, pp. 531-536.
- 622 53. Schwertmann, U. and Thalmann, H., (1976). The influence of [Fe (II)],[Si], and pH on the
623 formation of lepidocrocite and ferrihydrite during oxidation of aqueous FeCl₂ solutions, *Clay*
624 *Minerals*, 11, pp. 189-199.
- 625 54. Schwertmann U. and Cornell R. M. (2000). Iron Oxides in the Laboratory, 2nd ed.
626 Weinheim: Wiley-VCH.
- 627 55. Senko, J.M., Mohamed, Y., Dewers, T.A. and Krumholz, L.R., (2005a). Role for Fe (III)
628 minerals in nitrate-dependent microbial U (IV) oxidation, *Environmental Science &*
629 *Technology*, 39, pp. 2529-2536.
- 630 56. Senko, J.M., Dewers, T.A. and Krumholz, L.R., (2005b). Effect of oxidation rate and Fe (II)
631 state on microbial nitrate-dependent Fe (III) mineral formation, *Applied and Environmental*
632 *Microbiology*, 71, pp. 7172-7177.

- 633 57. Senn, D.B. and Hemond, H.F., (2002). Nitrate controls on iron and arsenic in an urban lake,
634 *Science*, 296, pp. 2373-2376.
- 635 58. Straub, K.L., Benz, M., Schink, B. and Widdel, F., (1996). Anaerobic, nitrate-dependent
636 microbial oxidation of ferrous iron, *Applied and Environmental Microbiology*, 62, pp. 1458-
637 1460.
- 638 59. Straub, K.L., Schönhuber, W.A., Buchholz-Cleven, B.E. and Schink, B., (2004). Diversity of
639 ferrous iron-oxidizing, nitrate-reducing bacteria and their involvement in oxygen
640 independent iron cycling, *Geomicrobiology Journal*, 21, pp. 371-378.
- 641 60. Sun, W., Sierra-Alvarez, R., Milner, L., Oremland, R. and Field, J.A., (2009). Arsenite and
642 ferrous iron oxidation linked to chemolithotrophic denitrification for the immobilization of
643 arsenic in anoxic environments, *Environmental Science & Technology*, 43, pp. 6585-6591.
- 644 61. Suzuki, T.M., Nonaka, T., Suda, A., Suzuki, N., Matsuoka, Y., Arai, T., Sato, S. and
645 Morikawa, T., (2017). Highly crystalline β -FeOOH (Cl) nanorod catalysts doped with
646 transition metals for efficient water oxidation, *Sustainable Energy & Fuels*, 1, pp. 636-643.
- 647 62. Takahashi, G., (2015). Sample preparation for X-ray fluorescence analysis III. Pressed Loose
648 Powder Methods, *Rigaku Journal*, 31, pp. 29-40.
- 649 63. Velenturf, A.P. and Jopson, J.S., (2019). Making the business case for resource recovery,
650 *Science of the Total Environment*, 648, pp. 1031-1041.
- 651 64. Villa-Gomez, D.K., Papirio, S., van Hullebusch, E.D., Farges, F., Nikitenko, S., Kramer, H.
652 and Lens, P.N.L., (2012). Influence of sulfide concentration and macronutrients on the
653 characteristics of metal precipitates relevant to metal recovery in bioreactors, *Bioresource*
654 *Technology*, 110, pp. 26-34.

- 655 65. Weber, K.A., Picardal, F.W. and Roden, E.E., (2001). Microbially catalyzed nitrate-
656 dependent oxidation of biogenic solid-phase Fe(II) compounds, *Environmental Science &*
657 *Technology*, 35, pp. 1644-1650.
- 658 66. Weber, K.A., Pollock, J., Cole, K.A., O'Connor, S.M., Achenbach, L.A. and Coates, J.D.,
659 (2006). Anaerobic nitrate-dependent Iron(II) biooxidation by a novel, lithoautotrophic,
660 *Betaproteobacterium*, strain 2002, *Applied and Environmental Microbiology*, 72, pp. 686-
661 694.
- 662 67. Xiu, W., Guo, H., Shen, J., Liu, S., Ding, S., Hou, W., Ma, J. and Dong, H., (2016).
663 Stimulation of Fe (II) oxidation, biogenic lepidocrocite formation, and arsenic
664 immobilization by *Pseudogulbenkiania* sp. strain 2002, *Environmental Science &*
665 *Technology*, 50, pp. 6449-6458.
- 666 68. Zhang, M., Zheng, P., Li, W., Wang, R., Ding, S. and Abbas, G., (2015). Performance of
667 nitrate-dependent anaerobic ferrous oxidizing (NAFO) process: a novel prospective
668 technology for autotrophic denitrification, *Bioresource Technology*, 179, pp. 543-548.
- 669 69. Zhao, L., Dong, H., Kukkadapu, R., Agrawal, A., Liu, D., Zhang, J. and Edelman, R.E.,
670 (2013). Biological oxidation of Fe(II) in reduced nontronite coupled with nitrate reduction by
671 *Pseudogulbenkiania* sp. Strain 2002, *Geochimica et Cosmochimica Acta*, 119, pp. 231-247.
- 672 70. Zou, G., Papirio S., van Hullebusch, E.D. and Puhakka (2015). Fluidized-bed denitrification
673 of mining water tolerates high nickel concentrations. *Bioresource Technology*, 179, pp. 284-
674 290.
- 675 71. Zou, G., Papirio, S., Lakaniemi, A.M., Ahoranta, S.H. and Puhakka, J.A., (2016). High rate
676 autotrophic denitrification in fluidized-bed biofilm reactors, *Chemical Engineering Journal*,
677 284, pp. 1287-1294.

678 **List of Tables**

679 **Table 1:** Color, FTIR/Raman spectroscopy bands and XRD phases of the precipitates obtained
680 during abiotic controls (AC), with different microbial cultures, i.e. *Thiobacillus*-mixed culture (TM),
681 *T. denitrificans* pure culture (TDP), activated sludge (AS) enrichment, and *Pseudogulbenkiania* sp.
682 2002 (PG), both with and without the addition of Cu, Ni and Zn.

683 **Table 2:** Elemental identification and quantitative compositional analysis by XRF and SEM-EDX
684 of the precipitates obtained in abiotic controls and in the batch bioassays operated with and without
685 heavy metals (Ni, Cu and Zn).

686 **Table 3:** Weight loss of calcined samples after thermal treatment at 650°C for 2 hours.

687

688

689

690

691

692

693

694

695

696

697

698

699 **List of Figures**

700 **Fig. 1:** Raman microscopy of the dark and red spots in the precipitates obtained from bottles
701 inoculated with the (A, B) *Thiobacillus*-mixed culture (TM) and (C, D) from abiotic controls.

702 **Fig. 2:** Raman spectra of the samples obtained during the experiments with (A) *Pseudogulbenkiania*
703 strain 2002 in the presence of Ni (PGN), (B) *Pseudogulbenkiania* strain 2002 (PG) and (C) activated
704 sludge in the presence of Cu (ASC).

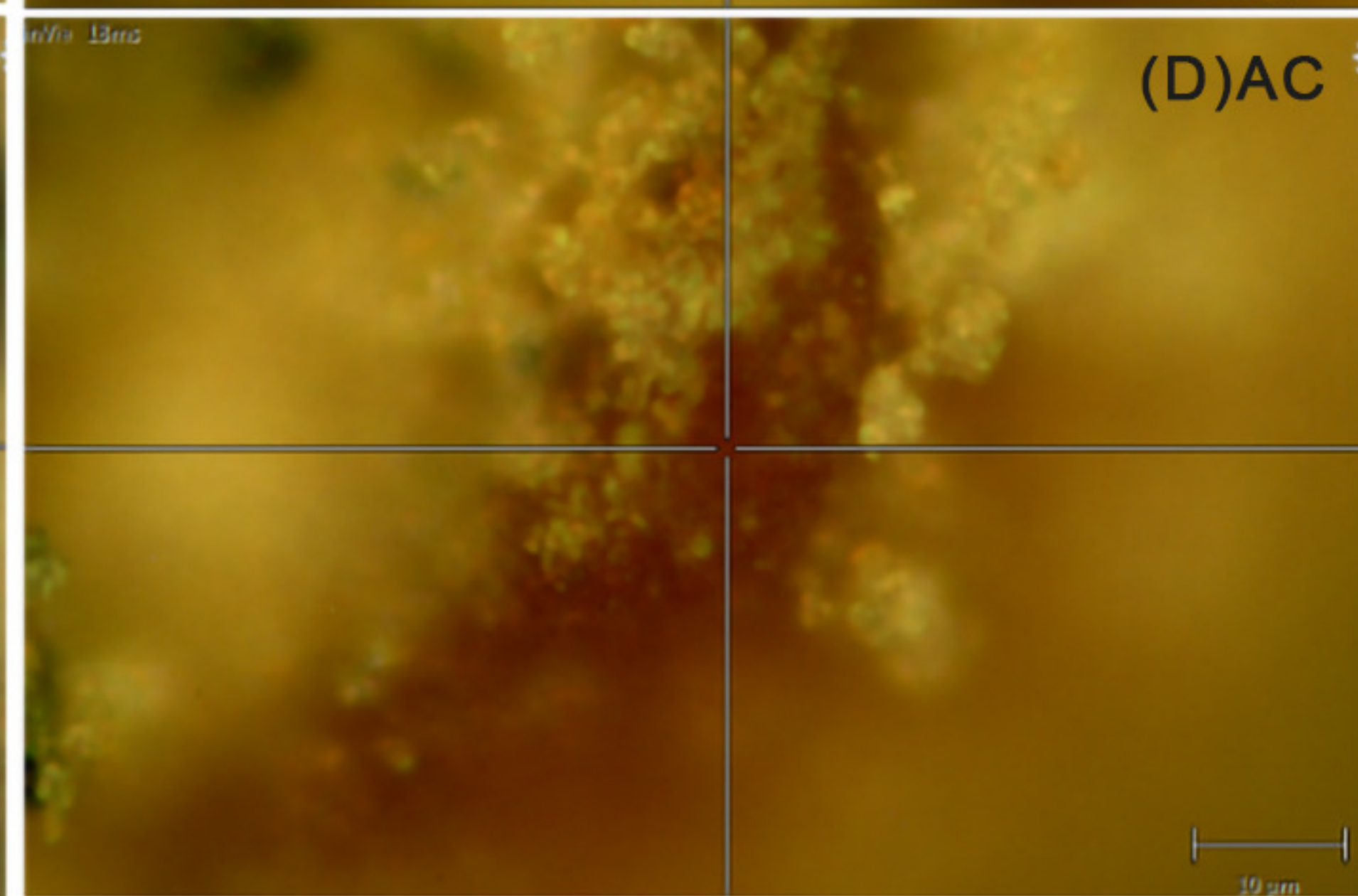
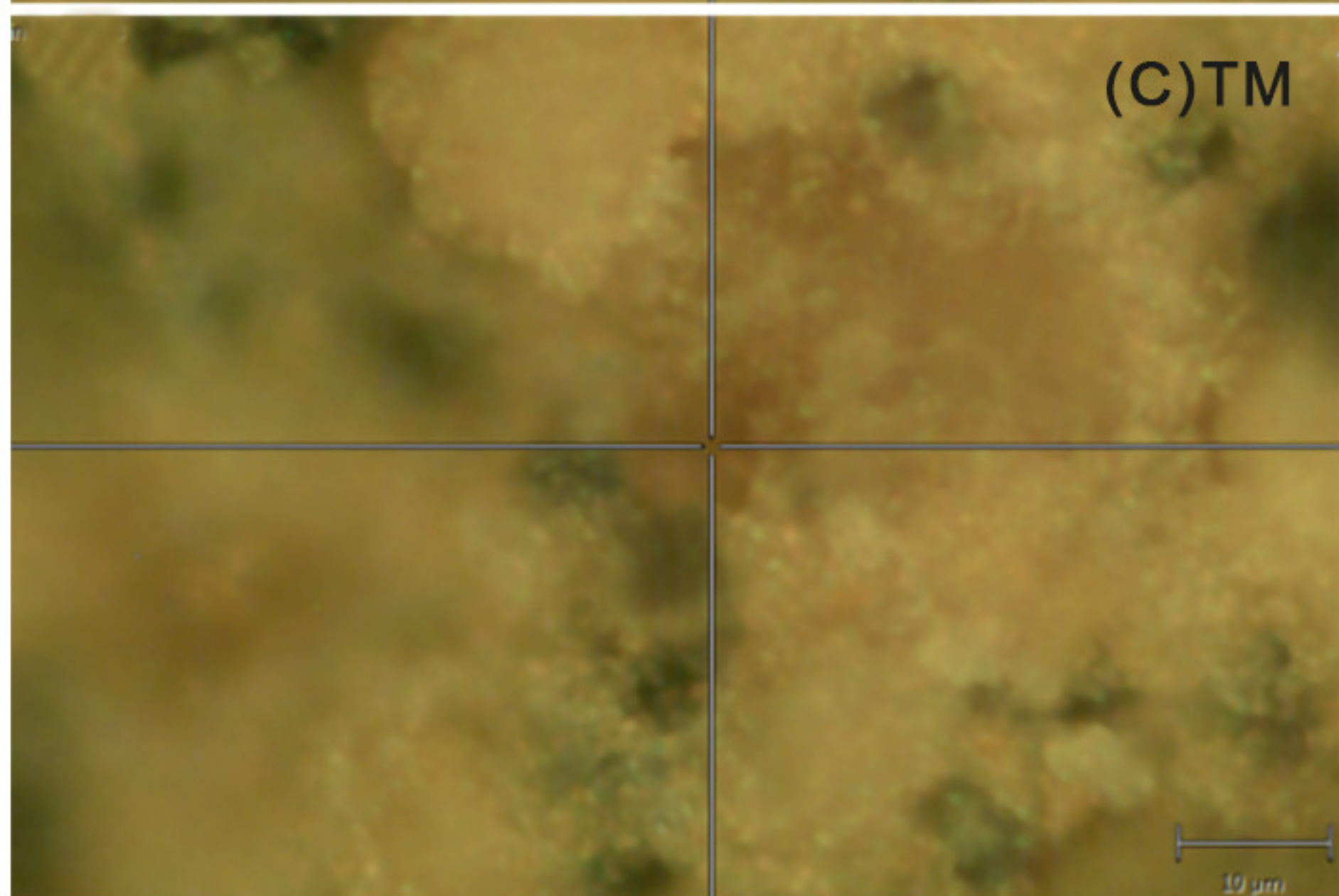
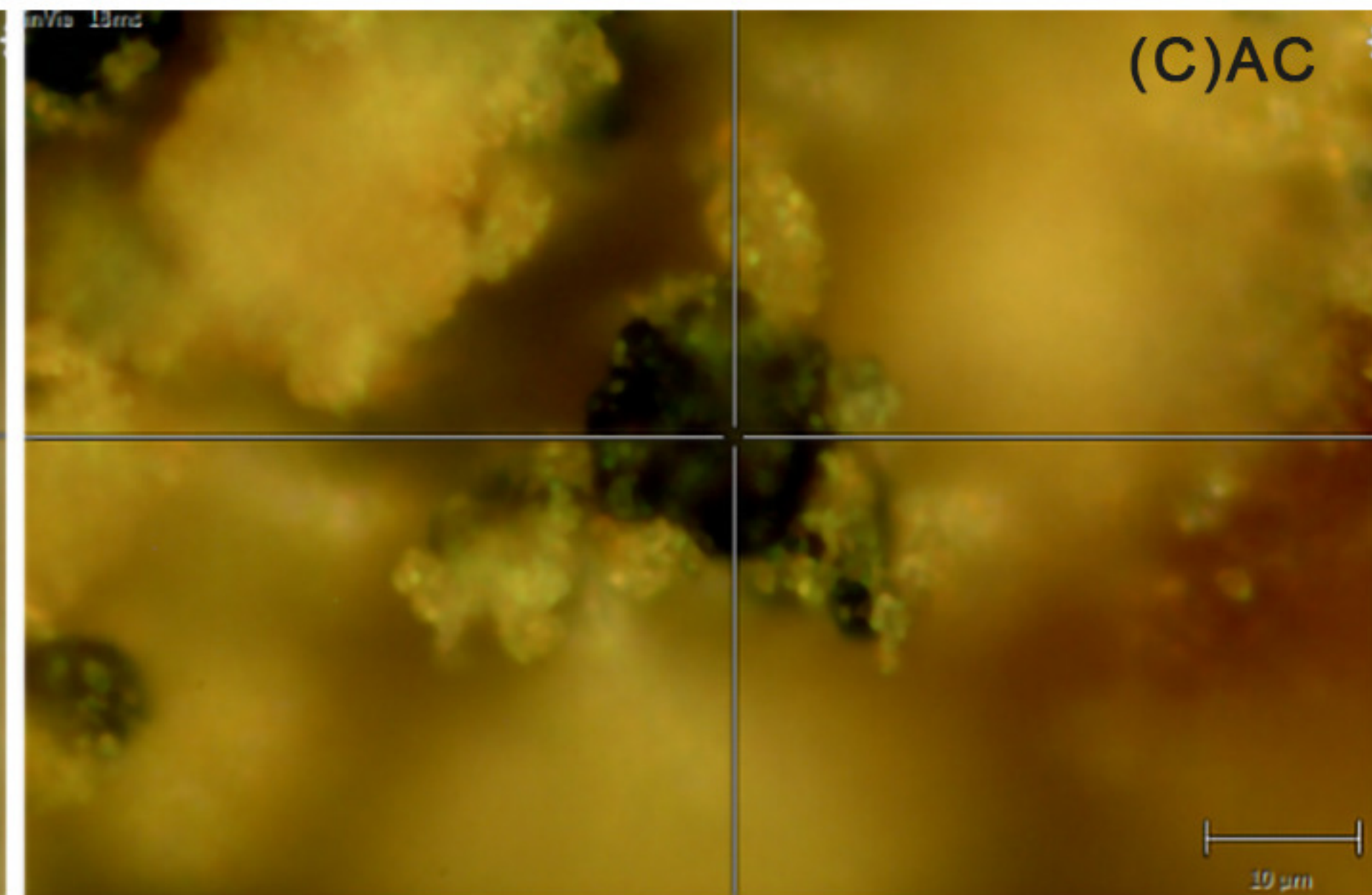
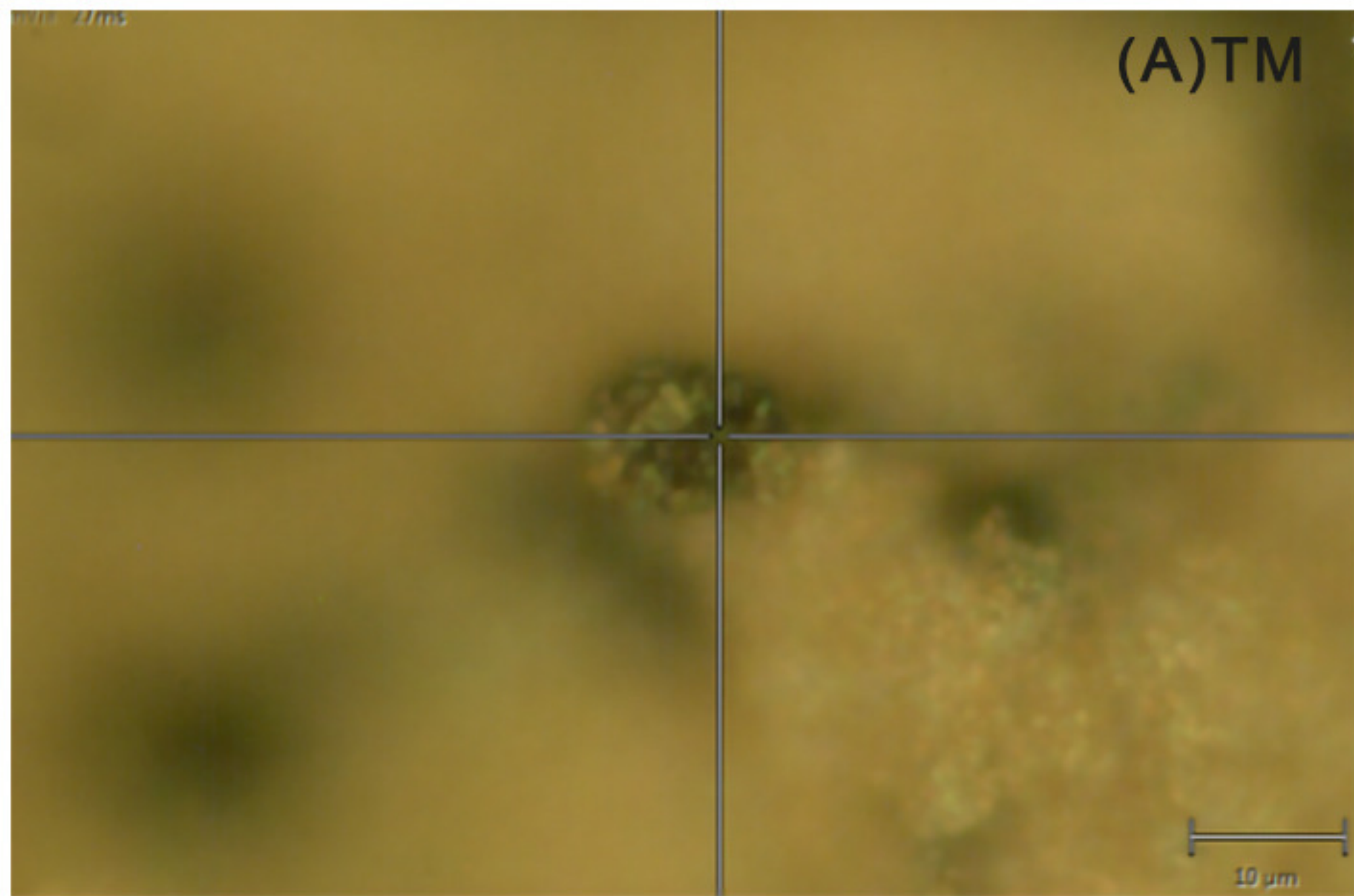
705 **Fig. 3:** SEM micrographs without coating of samples were obtained from (A) abiotic controls, and
706 from the bottles inoculated with (B) the *T. denitrificans* mixed culture, (C) *Pseudogulbenkiania*
707 strain 2002 and (D) *T. denitrificans* pure culture.

708 **Fig. 4:** SEM micrographs of samples obtained from abiotic controls (A), from the bottles inoculated
709 with *Thiobacillus*-mixed culture (B), with *Pseudogulbenkiania* strain 2002 in the presence of Ni (C)
710 and the precipitates obtained using activated sludge enrichment with addition of Cu (D, E).

711 **Fig. 5:** Mostly amorphous phases with a little amount of crystalline phases in XRD powder patterns
712 of TM (A), AS (B) and TMN (C) and ASN (D) samples (JPCDS card no.30-662)

713 **Fig. 6:** FTIR spectrum of the precipitates obtained during the abiotic controls, as representative of
714 those obtained with the microorganisms which showed a similar trend.

715 **Fig. 7:** XRD powder patterns of (A) PGC, (B) PGZ, (C) TM and (D) AS samples calcined at 650°C
716 for 2 h (JPCDS card no.30-662).



(A) AC

Siderite

Vivianite



(B) TM

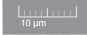
Amorphous phase

Crystalline phases



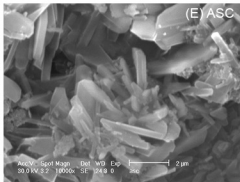
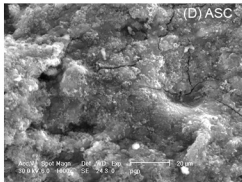
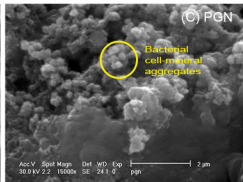
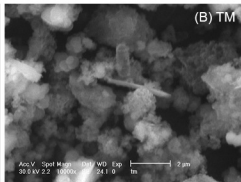
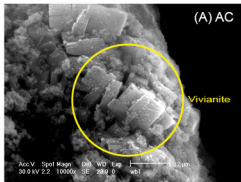
(C) PG

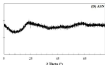
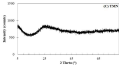
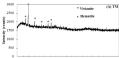
Bacterial cell-mineral aggregates

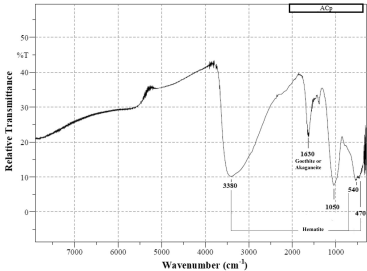


(D) TDP









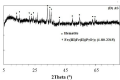
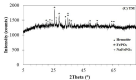
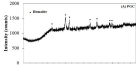


Table 1: Color, FTIR/Raman spectroscopy bands and XRD phases of the precipitates obtained during abiotic controls (AC), with different microbial cultures, i.e. *Thiobacillus*-mixed culture (TM), *T. denitrificans* pure culture (TDP), activated sludge (AS) enrichment, and *Pseudogulbenkiania* sp. 2002 (PG), both with and without the addition of Cu, Ni and Zn.

Sample	Color	FTIR, bands (cm ⁻¹)	Raman spectroscopy bands (cm ⁻¹)	Minerals (by FTIR/Raman Spectroscopy)	XRD phases	XRD phases at 650 °C
AC	Reddish	470, 540, 1050, 1630, 3380	Dark/Red: 225, 290-300, 412, 470, 611, 1000, 1321	Hematite (Goethite or Akaganeite)	Amorphous phases, Vivianite	Amorphous phases, Hematite, Fe ₂ (III)Fe(II)(P ₂ O ₇) ₂ (1-89-876)
TM	Red to brown	540, 1050, 1400, 1630, 3380	Dark: 225, 290-300, 412, 1000 Red: 400, 700	Hematite and Akaganeite (and/or Ferrihydrite)	Amorphous phases, Vivianite	Amorphous phases, Hematite, FePO ₄ , NaFePO ₄
TDP	Brownish-reddish, yellow	540, 1050, 1400, 1630, 3380	Dark: 225, 290-300, 412, 611, 1000 Red: 350, 700, 1300, 1600	Hematite and Maghemite and/or 2-line Ferrihydrite	Amorphous phases, Vivianite	Amorphous phases, Hematite, FePO ₄ , NaFePO ₄
AS	Dark reddish brown	540, 1050, 1630, 3380	Dark1: 225, 290-300, 412, 611 Dark2: 225, 290-300, 412, 700, 1000, 1300, 1600 Red: 350, 700, 1300, 1600 White: 350, 500, 700, 1350	Hematite, Maghemite and/or magnetite (and/or Ferrihydrite)	Amorphous phases, Vivianite, hematite	Amorphous phases, Hematite, Fe ₂ (III)Fe(II)(P ₂ O ₇) ₂ (1-80-2315))
PG	Brownish-reddish,	540, 1050, 1630, 3380	Dark: 225, 290-300, 470, 1000, 1600	Hematite and maghemite	Amorphous phases,	-

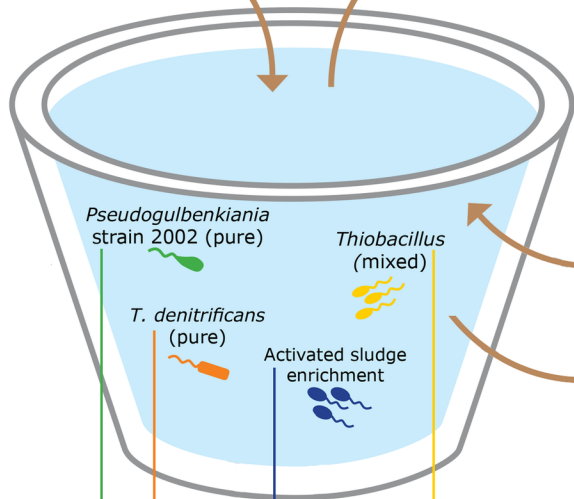
	yellow				Vivianite	
TMC	Red to brown (yellow)	470, 500, 540, 1050, 1400, 1630, 3448	Dark: 225, 290-300, 412, 1000 Red: 400, 700	Hematite and Akaganeite	Amorphous phases, $K_2CaP_2O_7$	-
TDPC	Brownish-reddish	470, 1050, 1400, 1630, 3380	Dark/red: 225, 400, 700, 1000, 1300	Hematite and Maghemite and/or 2-line Ferrihydrite	Amorphous phases	-
ASC	Brownish-reddish	470, 500, 1050, 1400, 1630, 3448	Dark1:225, 290-300, 412, 611 Dark2: 225, 290-300, 412, 700, 1000, 1300, 1600 Red: 400, 700, 1300, 1600 White: 400, 500, 700, 1350	Hematite, Maghemite and/or magnetite (and/or Ferrihydrite)	Amorphous phases, Hematite, $K_2CaP_2O_7$	Amorphous phases, Hematite, $NaFeO_2$ (1-76-600), Ca_3Cl_3P (1-84-1125)
PGC	Black	470, 1050, 1400, 1630, 3380	Dark: 400, 700, 1000, 1300	Hematite and maghemite	Amorphous phases	Amorphous phases, Hematite
TMN	Red to brown	450, 650, 940, 1630, 3430	Dark, red: 400, 700, 1000, 1321	Hematite Akaganeite/Ferrihydrite, and (possible Maghemite)	Amorphous phases	-
TDPN	Red to brown	450, 1050, 1400, 1630, 3380	Dark, red: 400, 700, 1000, 1321 Dark: Additional 1600	Hematite and Maghemite and/or 2-line Ferrihydrite	Amorphous phases	-

ASN	Red to brown	450, 1050, 1400, 1630, 3380	White: 400, 700, 1000, 1321, 1600	Hematite, Maghemite, (and/or Ferrihydrite)	Amorphous phases	-
PGN	Red to brown	450, 1050, 1400, 1630, 3430	Dark, red: 400, 700, 1000, 1321	Hematite and maghemite	Amorphous phases	Amorphous phases, Hematite
TMZ	Red to brown	410, 940, 1630, 3440	Dark, red: 225, 245, 411, 700, 1000, 1300	Hematite Akaganeite/Ferrihydrite, and (possible Maghemite)	Amorphous phases	-
TDPZ	Red to brown	450, 1050, 1400, 1630, 3380	Dark, red: 400, 700, 1000, 1321 Red/White: Additional 1600 (Maghemite)	Akaganeite and Hematite (possible Maghemite)	Amorphous phases	-
ASZ	Red to brown	450, 940, 1050, 1400, 1630, 3380	Dark, red: 400, 700, 1000, 1321 Red/White: Additional 1600 (Maghemite)	Hematite, Maghemite and/or magnetite (and/or Ferrihydrite)	Amorphous phases	-
PGZ	Black	450, 940, 1050, 1400, 1630, 3380	Dark, red: 225, 290-300, 412, 611, 700, 1000, 1321 Red/White: Additional 1600	Hematite and maghemite	Amorphous phases	Amorphous phases, Hematite

Table 3: Weight loss of calcined samples after thermal treatment at 650°C for 2 hours.

Sample	ACp	PGp	TMp	ASp	TDPp	PGCp	PGNp	PGZp	TMCp	ASCp
wt %	25.1	49.5	25.1	31.5	24.4	57.5	57.4	61.9	30.1	26.5

Nitrogen Pollution Removal



Biorecovery of Resources



Co-precipitation

Cu, Ni, Zn

Fe(III) Precipitates

Hematite, Maghemite

Hematite, Akaganeite

Maghemite

 Addition of Ni, Zn